Supporting Information

Integration of Image Preprocessing and Recognition Functions in an Optoelectronic Coupling Organic Ferroelectric Retinomorphic Neuristor

Qinyong Dai, Mengjiao Pei, Jianhang Guo, Qijing Wang, Ziqian Hao, Hengyuan Wang, Yating Li, Longfei Li, Kuakua Lu, Yang Yan, Yi Shi*and Yun Li*

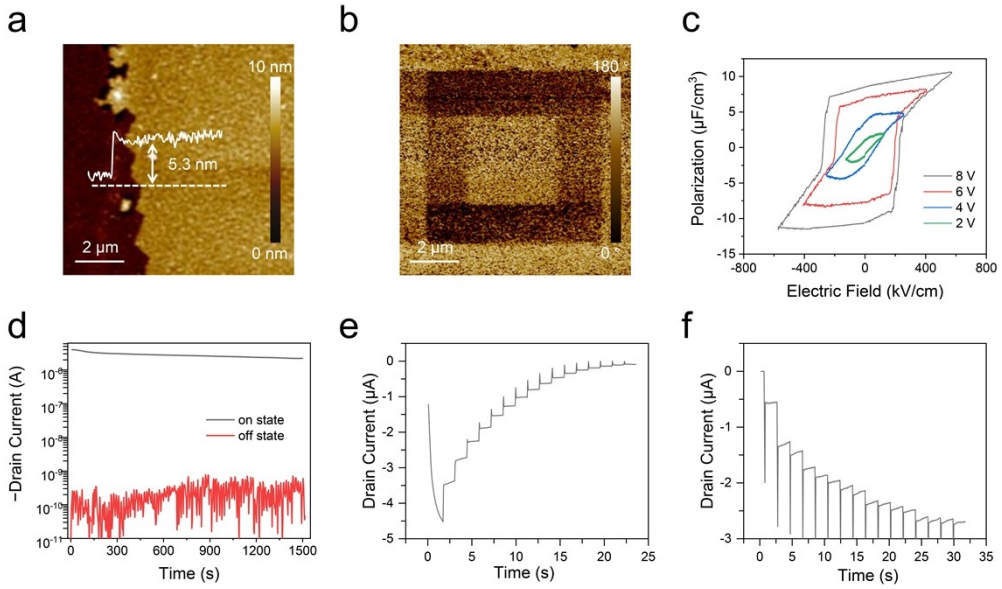

Fig. S1 Atomic force microscope (AFM), piezoresponse force microscopy (PFM), and polarization-voltage (*P-E*) loop characterizations of P(VDF-TrFE) thin films, and devices performance characterizations. (a) AFM height image and (b) piezoresponse force microscopy (PFM) out-of-plane phase images of the ultrathin P(VDF-TrFE) film. (c) The *P-E* hysteresis loops of P(VDF-TrFE) films with different sweeping ranges. (d) Retention measurements of the currents in the on and off states. (e) Realization of a long-term depression through positive gate pulses (width 10 ms, amplitude 5 V). (f) Realization of a long-term potentiation through negative gate pulses (width 10 ms, amplitude −10 V).

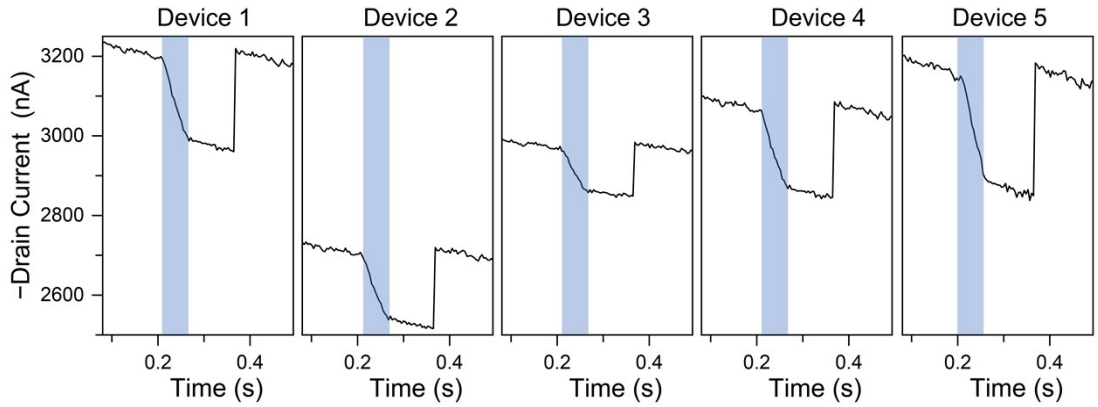

Fig. S2 Device variance of negative photoresponse in 5 different devices under light illumination at V_d = −1 V. Shadow areas represent the duration of light illumination.

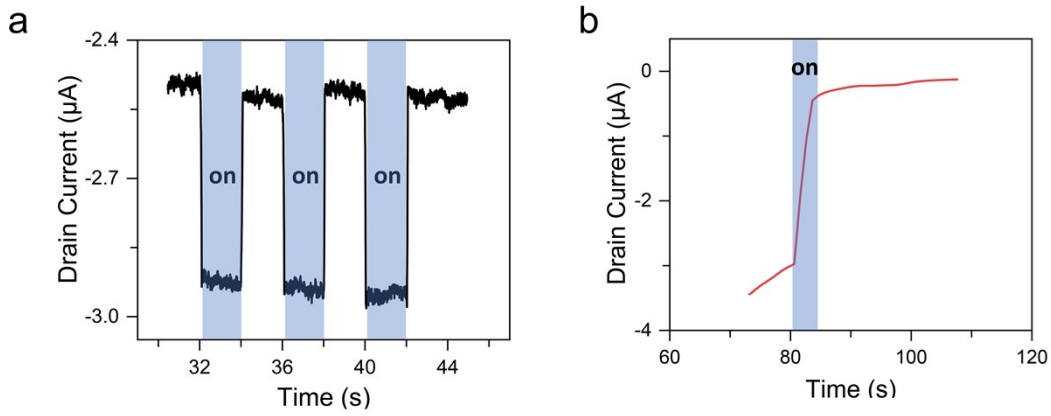

Fig. S3 A control experiment. (a) Photoresponse of the devices with PMMA layer. (b) Photoresponse of the devices without PMMA layer. The inset describes the extraction process of memory window.

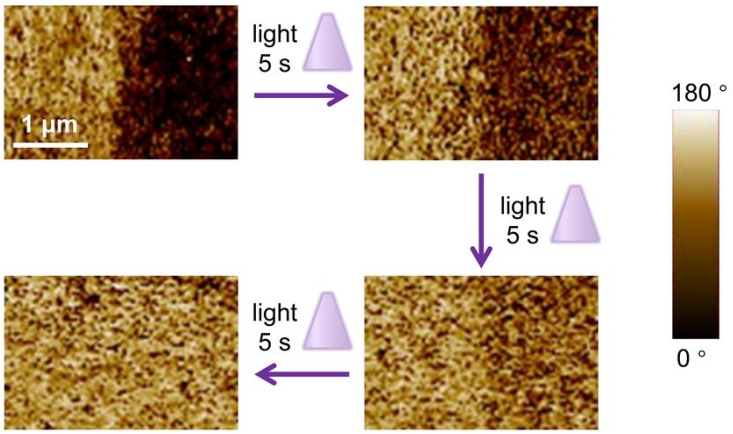

Fig. S4 The PFM phase diagrams of the devices as a function of the light exposure time (wavelengths of 365 nm, intensity of approximately 10 mW/cm^2).

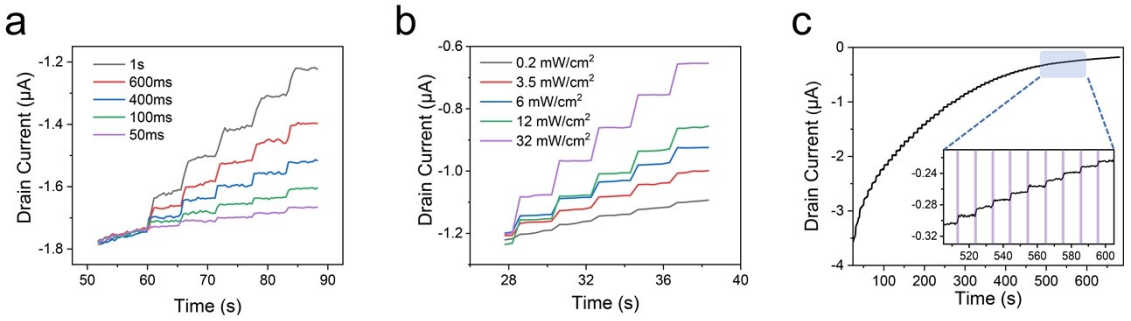

Fig. S5 The multi-level memory characteristics. (a) Time-dependent drain current under five light pulses (365 nm, 3.5 mW/cm^2) with different exposure times of 0.05, 0.1, 0.4, 0.6, and 1 s. (b) Time-dependent drain current under five light pulses (365 nm, 400 ms) with different optical powers. (c) Multilevel storage capability characterization (64 states) under light pulses (365 nm, 3.5 mW/cm^2, 400 ms) every 10 s.

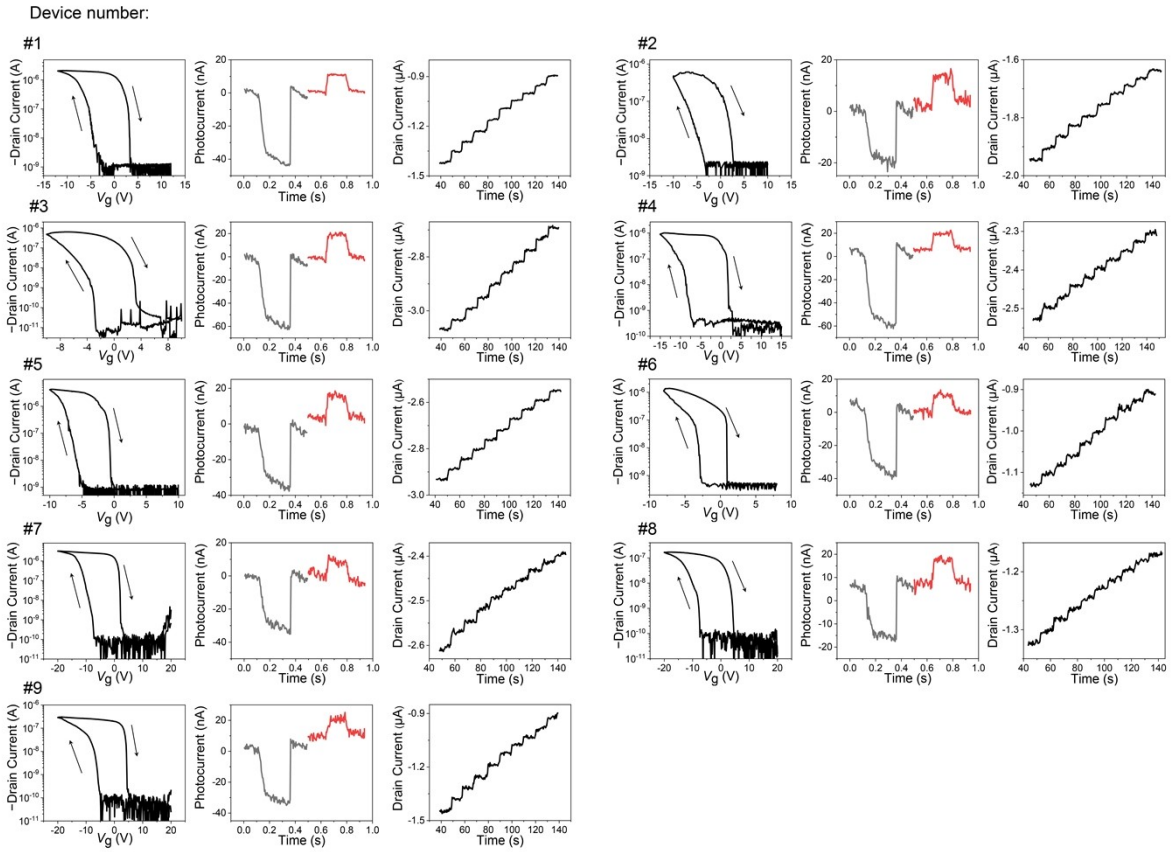

Fig. S6 Transfer curves, bidirectional photoresponse characteristics, and multi-level memory characteristics by optical modulation of the 9 devices.

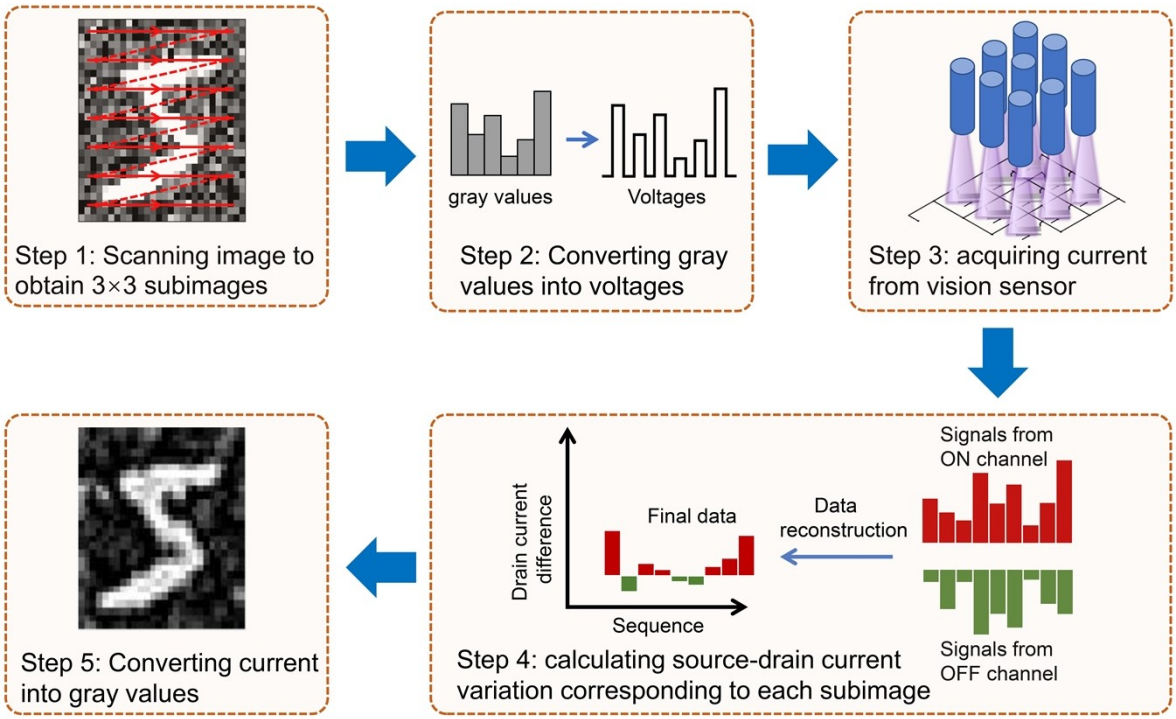

Fig. S7 The specific operation process of image preprocessing.

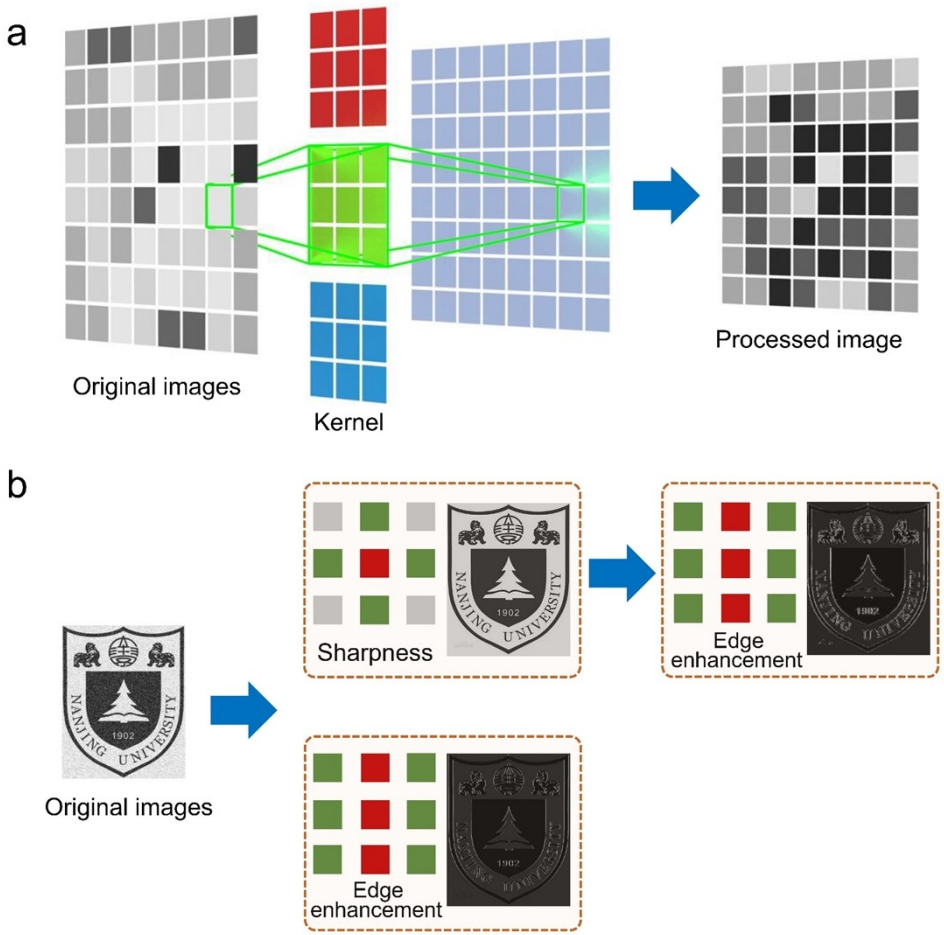

Fig. S8 Reconfigurable retinomorphic vision sensor for simultaneous image sensing and processing. (a) Vision sensor for simultaneous image sensing and processing. (b) Demonstration of image processing with different operations (i.e., edge enhancement and sharpness). These operations are realized by controlling the photoresponse of each pixel in the sensor by varying V_g independently.

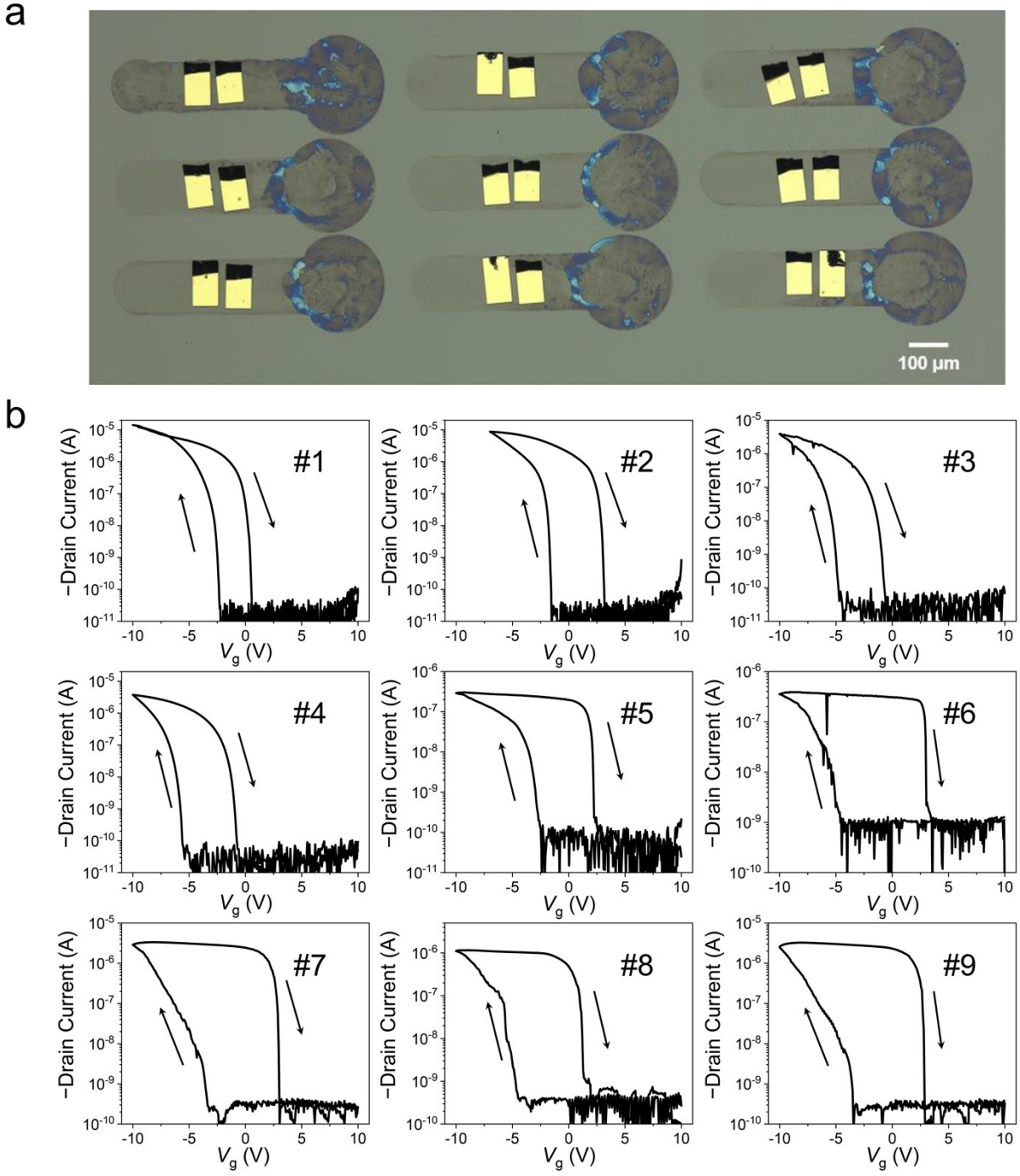

Fig. S9 (a) Optical microscope image and (b) transfer curves of the 3×3 organic ferroelectric retinomorphic neuristors-based sensor array.

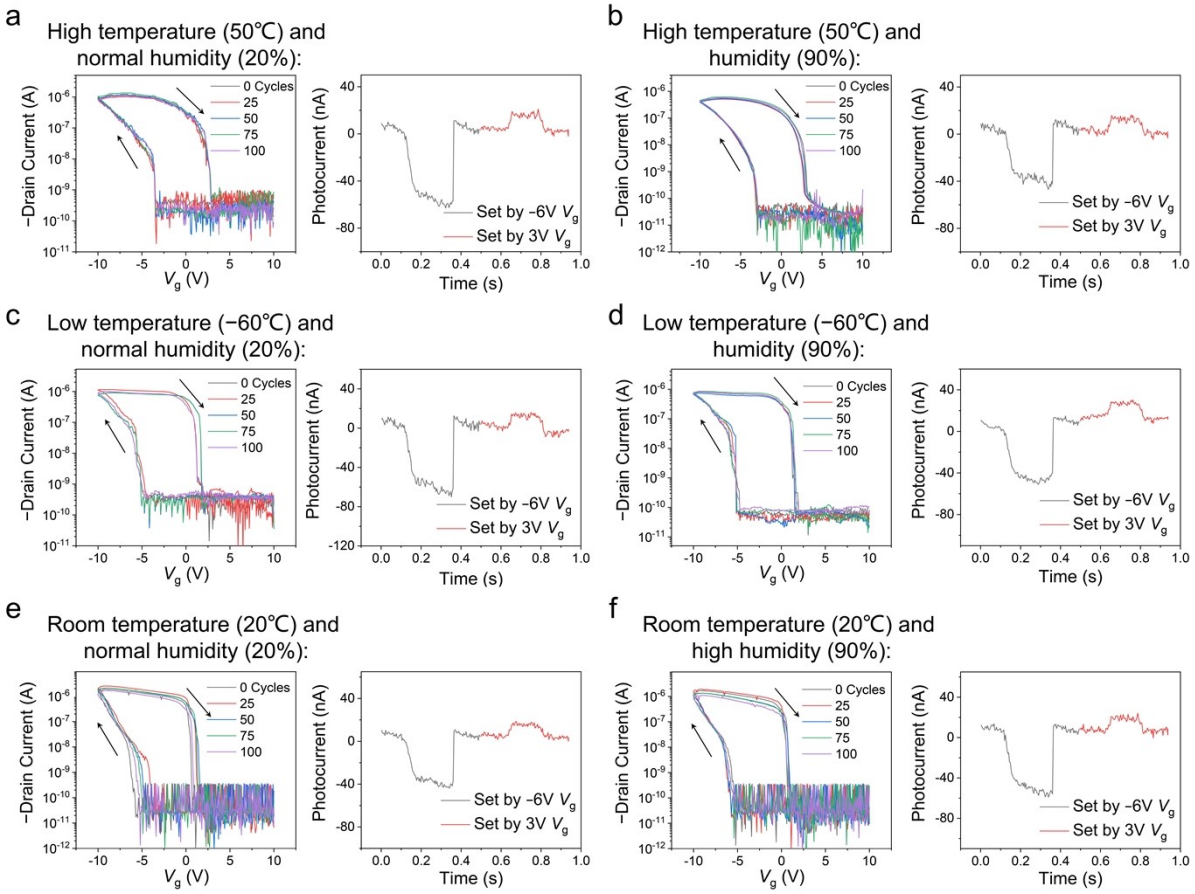

Fig. S10 The stability measurements of our devices encapsulated by the parylene films in harsh environments. The testing time for 100 cycles is one hour. (a) High temperature (50 °C) and normal humidity (20 %), (b) high temperature (50 °C) and humidity (90 %), (c) low temperature (−60 °C) and normal humidity (20 %), (d) low temperature (−60 °C) and humidity (90 %), (e) room temperature (20 °C) and normal humidity (20 %), (f) room temperature (20 °C) and high humidity (90 %).

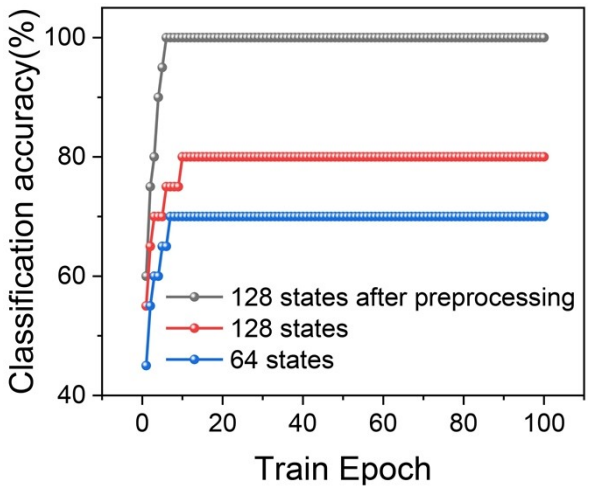

Fig. S11 Comparison of classification recognition rates using different states with and without preprocessing.

Table S1. Comparison among the recently developed image recognition systems based on different devices. CNN: convolutional neural network; FCNN: full-connected neural network.

Materials system	Structure	Function	Network type	Accuracy	Ref.
Pyr-GDY/Graphene/Pb	photodiode	recognition	FCNN	90%	1
$MoS_2/PtTe_2$	transistor	recognition	FCNN	80%	2
Graphene/WSe_2	transistor	recognition	CNN	72%	3
Graphene/MoS_2	transistor	recognition	FCNN	92%	4
HfS_2	transistor	recognition	CNN	88%	5
C_8-BTBT/F_{16}CuPc	a two-terminal synapse	preprocessing	-	-	6
Graphene/PM6:Y6	transistor	retinomorphic preprocessing	-	-	7
Wse_2	a two-terminal synapse	retinomorphic preprocessing	-	-	8
PDPP3T:PCBM	transistor	visual adaption	-	-	9
In_2O_3	transistor	visual adaption	-	-	10
MoS_2	transistor	visual adaption & recognition	CNN	96%	11
α-In_2Se_3	transistor	visual adaption & recognition	CNN	93%	12
MoS_2/LSMO	transistor	preprocessing & recognition	CNN	90%	13
ZnO + Mo/SiO_2/W	transistor + memristor	preprocessing & recognition	FCNN	99%	14
MoO_3/Pd/SiO_2	random access memory	preprocessing & recognition	CNN	99%	15
BP	transistor	preprocessing & recognition	CNN	92%	16
WSe2/h-BN + HfO_x	transistor + memristor	retinomorphic preprocessing & recognition	CNN	100%	17
C_8-BTBT/PMMA/P(VDF-TrFE)	transistor	retinomorphic preprocessing & recognition	CNN	90%	this work

Materials and Methods

Fabrication of P(VDF-TrFE) and C_8-BTBT films

HfO_2 with a thickness of 25 nm was deposited on highly doped n-type Si substrates by atomic layer deposition technology. Then, the substrates were ultrasonically cleaned with acetone, isopropanol and deionized water for 15 minutes. P(VDF-TrFE) (70:30 molar ratio) purchased from Solvay Inc. was dissolved in a mixture of DMF, and the counter solvent p-anisaldehyde (0.5 wt%) at a concentration of 0.5 wt%. 3.5 μL solution was dropped onto the substrate. Moreover, a P(VDF-TrFE) film was obtained with antisolvent-assisted crystallization technology under nitrogen conditions. The substrate with P(VDF-TrFE) was left standing in nitrogen for 12 hours to fully evaporate the solvent. C_8-BTBT (0.5 wt%) and PMMA (0.1 wt%) were dissolved in a mixture of anisole and p-anisaldehyde (0.5 wt%). Subsequently, PMMA/C_8-BTBT thin films were formed on the P(VDF-TrFE) layer through vertical phase separation by the same method.

Device Fabrication

Au electrodes with a thickness of 100 nm and an area of 30 × 90 μm^2 were transferred onto C_8-BTBT films as source and drain electrodes. The channel length and width of the devices were defined as 80 and 20 μm, respectively.

Electrical and Optoelectrical Characterizations of Organic Ferroelectric Retinomorphic Neuristors

A semiconductor device analyzer (Agilent B1500) was used to test the electrical characteristics of the devices under vacuum conditions of 10^{-3} Torr. A 365 nm ultraviolet light emitting diode (LED) was used as the light source to measure the optoelectrical performance of the devices, where the light pulse signal was generated by a signal generator. AFM characterizations were performed using a scanning probe microscope (SPA-400) controlled by an SPI 4000 probe station (Seiko Instruments). PFM characterizations were performed with an Asylum Research Cypher scanning probe microscope (Asylum Research, Oxford Instruments, China). ions. *P-E* hysteresis loops were performed with a PREMIER II ferroelectric analyzer.

References

1 Y. X. Hou, Y. Li, Z. C. Zhang, J. Q. Li, D. H. Qi, X. D. Chen, J. J. Wang, B. W. Yao, M. X. Yu, T. B. Lu and J. Zhang, *ACS Nano*, 2021, **15**, 1497–1508.

2 M. M. Islam, A. Krishnaprasad, D. Dev, R. Martinez-Martinez, V. Okonkwo, B. Wu, S. S. Han, T. S. Bae, H. S. Chung, J. Touma, Y. Jung and T. Roy, *ACS Nano*, 2022, **16**, 10188–10198.

3 S. H. Kim, M. U. Park, C. Lee, S. G. Yi, M. Kim, Y. Choi, J. H. Cho and K. H. Yoo, *Nanoscale Adv.*, 2021, **3**, 4952–4960.

4 J. Yu, X. Yang, G. Gao, Y. Xiong, Y. Wang, J. Han, Y. Chen, H. Zhang, Q. Sun and Z. L. Wang, *Sci. Adv.*, 2021, **7**, eabd9117.

5 H. Xiong, L. Xu, C. Gao, Q. Zhang, M. Deng, Q. Wang, J. Zhang, D. Fuchs, W. Li, A. Cui, L. Shang, K. Jiang, Z. Hu and J. Chu, *ACS Appl. Mater. Interfaces*, 2021, **13**, 50132–50140.

6 Z. Hao, H. Wang, S. Jiang, J. Qian, X. Xu, Y. Li, M. Pei, B. Zhang, J. Guo, H. Zhao, J. Chen, Y. Tong, J. Wang, X. Wang, Y. Shi and Y. Li, *Adv. Sci.*, 2022, **9**, eabd9117.

7 C. Han, X. Liu, X. Han, M. He, J. Han, H. Zhang, X. Hou, H. Zhou, H. Yu, Z. Wu, J. Gou and J. Wang, *Adv. Funct. Mater.*, 2022, **32**, 2209680.

8 L. Mennel, J. Symonowicz, S. Wachter, D. K. Polyushkin, A. J. Molina-Mendoza and T. Mueller, *Nature*, 2020, **579**, 62–66.

9 Z. He, H. Shen, D. Ye, L. Xiang, W. Zhao, J. Ding, F. Zhang, C. an Di and D. Zhu, *Nat. Electron.*, 2021, **4**, 522–529.

10 C. Jin, W. Liu, Y. Xu, Y. Huang, Y. Nie, X. Shi, G. Zhang, P. He, J. Zhang, H. Cao, J. Sun and J. Yang, *Nano Lett.*, 2022, **22**, 3372–3379.

11 F. Liao, Z. Zhou, B. J. Kim, J. Chen, J. Wang, T. Wan, Y. Zhou, A. T. Hoang, C. Wang, J. Kang, J. H. Ahn and Y. Chai, *Nat. Electron.*, 2022, **5**, 84–91.

12 Y. Cai, F. Wang, X. Wang, S. Li, Y. Wang, J. Yang, T. Yan, X. Zhan, F. Wang, R. Cheng, J. He and Z. Wang, *Adv. Funct. Mater.*, 2022, **33**, 2212917.

13 J. Du, D. Xie, Q. Zhang, H. Zhong, F. Meng, X. Fu, Q. Sun, H. Ni, T. Li, E. jia Guo, H. Guo, M. He, C. Wang, L. Gu, X. Xu, G. Zhang, G. Yang, K. Jin and C. Ge, *Nano Energy*, 2021, **89**, 106439.

14 B. Dang, K. Liu, X. Wu, Z. Yang, L. Xu, Y. Yang and R. Huang, *Adv. Mater.*, 2022, **22**, 2204844.

15 F. Zhou, Z. Zhou, J. Chen, T. H. Choy, J. Wang, N. Zhang, Z. Lin, S. Yu, J. Kang, H. S. P. Wong and Y. Chai, *Nat. Nanotechnol.*, 2019, **14**, 776–782.

16 S. Lee, R. Peng, C. Wu and M. Li, *Nat. Commun.*, 2022, **13**, 1485.

17 S. Wang, C. Y. Wang, P. Wang, C. Wang, Z. A. Li, C. Pan, Y. Dai, A. Gao, C. Liu, J. Liu, H. Yang, X. Liu, B. Cheng, K. Chen, Z. Wang, K. Watanabe, T. Taniguchi, S. J. Liang and F. Miao, *Natl. Sci. Rev.*, 2021, **8**, 10–14.